Induced ordering in electrodeposited nanocrystalline Ni–Mn alloys

A. Stephen,[1,4,a] F. Rossi,[1] L. Nasi,[1] C. Ferrari,[1] N. Ponpandian,[2] M. V. Ananth,[3] and V. Ravichandran[4]
[1]*IMEM-CNR Institute, Parco Area delle Scienze 37/A, I-43100 Parma, Italy*
[2]*Institute of Physics, University of Rostock, Universitätsplatz 3, 18051 Rostock, Germany*
[3]*Electrochemical Energy Sources Division, Central Electrochemical Research Institute, Karaikudi 630 006, India*
[4]*Material Science Centre, Department of Nuclear Physics, University of Madras, Guindy Campus, Chennai 600 025, India*

(Received 10 April 2007; accepted 16 December 2007; published online 10 March 2008)

The Ni_3Mn type of ordering in nanocrystalline NiMn films with different compositions prepared by electrodeposition was investigated by using x-ray diffraction, differential scanning calorimetry (DSC), thermogravimetric analyzer, Mössbauer spectroscopy, and transmission electron microscopy. The investigations reveal the existence of composition-induced Ni_3Mn-type ordering in the as-deposited film of 76.2 at. % Ni. The atomic disorder is characterized by an exothermic effect in DSC. An analysis of the broad exothermic transition reveals the stages of phase transformation leading to ordering. The Curie temperatures of the alloys were determined from thermomagnetic measurements, the maximum value obtained for the ordered sample. Mössbauer spectroscopy at room temperature reveals ordered (ferromagnetic) and disordered (paramagnetic) phases in the as-deposited films. Superlattice reflections observed in selected area electron diffraction pattern for the 76.2 at. % Ni film alone further support the observation of composition-specific atomic ordering. © *2008 American Institute of Physics*. [DOI: 10.1063/1.2844211]

I. INTRODUCTION

Electrodeposition is an important cost-effective, rapid method for preparing pure nanocrystalline metals and alloys as films or in bulk form. Ni–Mn alloy system has attracted significant attention of researchers recently. The Ni–Mn based electrodeposited alloys have been developed for magnetic microelectromechanical systems (MEMSs) including magnetic sensors, actuators, and recording heads.[1,2] Scientists have prepared many devices by the UV-LIGA (from the German acronym lithographie galvanoformung und abformung or in English lithography, electroplating, and molding) technique.[3] High-strength and temperature resistant electrodeposited Ni films for LIGA and MEMS applications were obtained by the incorporation of small amounts of Mn, which significantly increases the recrystallization temperature, contributing to the thermal stability of the alloys. The spectacular increase in the bit density of magnetic disks has been achieved by giant magnetoresistance and spin valve reading heads, that require soft ferromagnetic thin films with acceptable corrosion resistance, as in NiMn films.[4,5] Further, inverse magnetocaloric effect has been reported in a number of Ni–Mn based systems.[6] Since the as-prepared films show disordered structure, prolonged annealing treatments are generally required to get the ordered structure ($L1_2$) and exploit their characteristic properties. The disorder-order transition degrades the performance of the devices, since the physical properties of the alloys change profoundly when subjected to mechanical and thermal treatments. During ordering, atoms of one kind move to a particular site forming an ordered arrangement having a lower potential energy than the disordered one. Thus atomic disorder is a source of energy storage.[7] Electrodeposited alloys exhibit interesting structural peculiarities[8–10] inherent to the very process. Electrodeposition yields additional phases and co-deposits[11] with various microstructural features.[12–14]

The disordered phases in ball-milled Ni_3Si and Ni_3Al is revealed by exothermic heat effects through differential scanning calorimetry (DSC) technique.[15–17] Recently Huang[18] reported metastable phases and phase transformations in sputtered NiMn films using DSC. Many extensive investigations have been carried out on Ni_3Mn alloy by magnetization, neutron diffraction, and electron microscopy techniques to investigate the ordering process and its effect on magnetic properties.[19–21] Chandra and Radhakrishnan[22] have carried out Mössbauer investigations in thermally prepared Ni–Mn alloys, for a range of compositions. Kaya and Nakayama[23] have measured the specific heat of Ni_3Mn alloy after annealing at various temperatures, and estimated the energy of ordering. The coexistence of disordered and ordered phases in partially ordered Ni_3Mn alloys was confirmed by neutron diffraction[24–26] and electron microscopy[27] investigations. Magnetoresistance and electrical resistance measurements have also been studied.[28–30] The reentrant spin glass effect was studied by a number of researchers.[31–34] Starting from the early observations by Kaya and Kussmann[35] and Sidorov and Doroshenko,[36] several studies have concentrated on the ordering process in the range of Ni of 60%–80%. The author has discussed the role of deposition parameters and the magnetic properties of electrodeposited Ni–Mn alloys elsewhere.[37,38] This work presents a study of the influence of alloy composition in structural ordering in electrodeposited

[a]Author to whom correspondence should be addressed. Electronic mail: stephen_arum@hotmail.com.

TABLE I. Sample label, bath composition, current density (CD), Ni atomic percentage, and Curie temperature (T_C).

Deposit No.	Bath composition (gl^{-1})		CD ($mA\ cm^{-2}$)	Ni at. %	T_C (K)
	$NiSO_4H_2O$	$MnSO_4H_2O$			
1	40	150	30	72.4	607
2	100	150	30	76.2	626
3	150	150	30	79.0	620
4	150	50	30	82.4	614
5	150	50	60	85.8	618
6	150	50	80	87.5	619
7	150	25	30	92.1	617

nanocrystalline Ni_xMn films with x in the range of 71%–92%, various compositions obtained by changing the deposition parameters such as current densities (CDs) and bath compositions. The study reveals the existence of a composition-induced ordering behavior in electrodeposited Ni–Mn films.

II. EXPERIMENT

The Ni–Mn alloys were electrodeposited on a pretreated stainless steel substrate at RT from simple acidic sulphate baths of *p*H 3.0. The details have been described elsewhere.[38] The deposition CD was generally maintained at 30 $mA\ cm^{-2}$ except for one bath where deposits were obtained also at higher CDs of 60 and 80 $mA\ cm^{-2}$. In all depositions 50 $g\ l^{-1}$ of $(NH_4)_2\ SO_4$ was used as bath additive. The deposits were mechanically removed as flakes/foils for further investigations. Their compositions were determined by standard chemical analyses and energy dispersive x-ray analysis. The DSC studies were carried out on a Perkin–Elmer DSC-7 in argon atmosphere. The thermomagnetic measurements were carried out on a thermogravimetric analyzer Perkin–Elmer TGA-7, using a horse shoe magnet. The scans were repeated more than once for ensuring reproducibility. X-ray diffraction (XRD) measurements were carried out using Cu $K\alpha_1$ radiation on a Guinier-type diffractometer from Huber Diffraktionstechnik. The Mössbauer spectra at RT were recorded using a Wissel constant acceleration spectrometer with $^{57}Co(Rh)$ source. The samples for Mössbauer spectroscopy were prepared by adding 5 $g\ l^{-1}$ of $FeSO_4(NH_4)_2SO_4 \cdot 6H_2O$ to the baths in order to introduce Fe in the alloys. The deposits were powdered and mixed with boron nitride in the approximate ratio of 1:10 in weight to control the gamma ray absorption. Results of Mössbauer measurements suggested that Fe atoms were completely dissolved into the alloys. Transmission electron microscopy (TEM) was carried out in a JEOL 2000FX microscope working at 200 kV, after subjecting the samples to Ar^+ ion milling.

III. RESULTS AND DISCUSSION

A. Structural analysis

The alloy composition and the Curie temperature (T_C) of the deposits from various bath compositions and CDs are listed as Table I. The structures of all the alloys were investigated by XRD and found to conform to an A_3B fcc structure with $a=3.5239(4)$ Å, almost independent of Ni atomic percentage. The XRD pattern obtained for an alloy with 82.4 at. % Ni shown in Fig. 1 is a typical example. Relative intensities of the peaks $I_{(111)}:I_{(200)}:I_{(220)}:I_{(311)}:I_{(222)} = 100:28:14:10:4$ obtained from the profiles match well with those calculated for the Ni_3Mn alloy. The average crystallite size was 26 nm as determined from x-ray line broadening analysis and later confirmed by the TEM measurements for all deposits made at a CD of 30 $mA\ cm^{-2}$. Figure 2(a) corresponding to deposit No.2 is typical of the bright field TEM micrographs obtained for the deposits, and the grain size distribution extracted therefrom is shown as Fig. 2(b). However, the crystallite size decreases, considerably for higher CDs, to as low as 8 nm at a CD of 80 $mA\ cm^{-2}$.

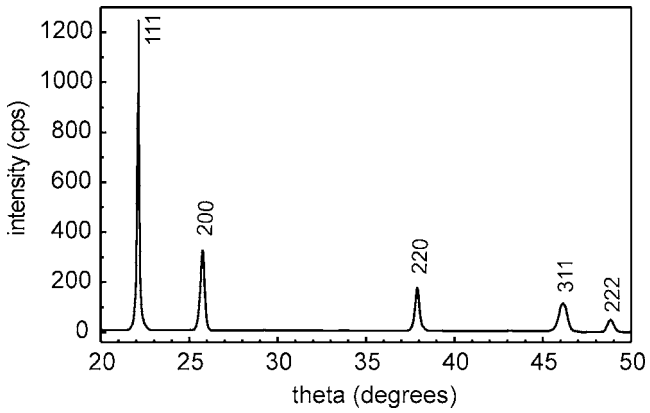

FIG. 1. The room temperature x-ray diffraction pattern for the deposit with 82.4 at. % of Ni.

B. DSC studies

The DSC scans of all the samples were typically done at a heating rate of 10 K/min, except in one case where an additional slow scan was performed. Figures 3(a) and 3(b) are DSC traces obtained, respectively, for the 72.4 (deposit No. 1) and 76.2 (deposit No. 2) at. % Ni alloys, while the thermograms for a few other deposits are shown stacked in Fig. 3(d). The thermal behavior of these electrodeposited samples differs considerably from those of Ni_3Si, Ni_3Al milled alloys[15,16] and sputtered Ni–Mn thin films.[18,39] All the DSC thermographs except for the case of 76.2 at. % Ni [Fig. 3(b)] present two endothermic peaks, one at ~570 K and the other above 833 K. An endothermic peak (Endo I), the Curie transition (T_C) of the alloy, and the broad exothermic region with fine features followed by a second endothermic peak (Endo II) are marked in Fig. 3(c). The first endothermic peak in the DSC thermograms is attributed to hydrogen desorption. The hydrogen inclusion is known to be an inevitable co-process of electrodeposition. DSC is a powerful tool to study the desorption of hydrogen as an endothermic process.[40,41]

For alloys with Ni content ranging from 72.4 to 41 at. %, broad exothermic regions in the region of 623–833 K are also noticed in Fig. 3. Since ordering is known to occur for Ni–Mn alloys somewhere in the range of 60 to 82 at. % of Ni,[35,42] this exothermic region was investi-

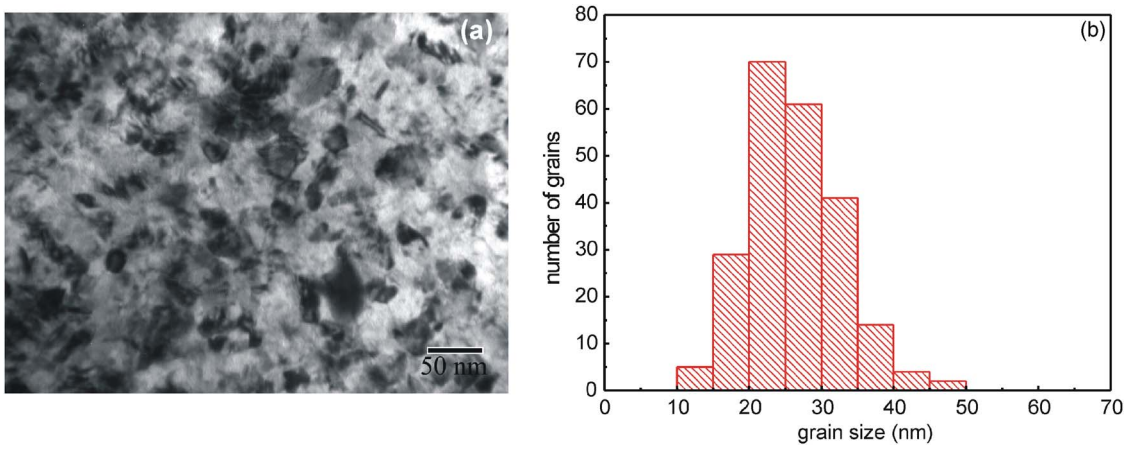

FIG. 2. (Color online) TEM bright field image (a) and the corresponding grain size distribution (b) of the 76.2 at. % Ni sample.

gated further. In order to understand the hidden features of the broad exothermic region observed, the DSC scan for the sample with 82.4 at. % Ni was repeated at a slower heating rate of 5 K/min. This is shown in Fig. 3(c). The thermograph clearly shows that the broad exothermic region, in fact, consists of three component profiles, marked as Exo I, II, and III. For all the samples the exothermic part of the DSC profile could, in fact, be fitted with three Gaussian distributions, suggesting the operation of three individual processes. The presence of such components in the exothermic peak of disorder-order transition has also been observed in the DSC scans of several ball-milled nanocrystalline intermetallic compounds.[14–16,43] These components indicate that the progression of the structural transition toward an ordered state has three distinct stages. On the basis of literature models,[18,43] these exothermic components are sequentially attributed to the relaxation of defects and stresses (Exo I), progression of a long-range ordering (Exo II) and crystallite growth from the nanocrystalline to microcrystalline regime (Exo III). The individual energy values for the above processes were calculated to be −10.2, −16.7, and −4.6 kJ/mol, respectively, for the sample with 76.2 at. % Ni and −16.2,

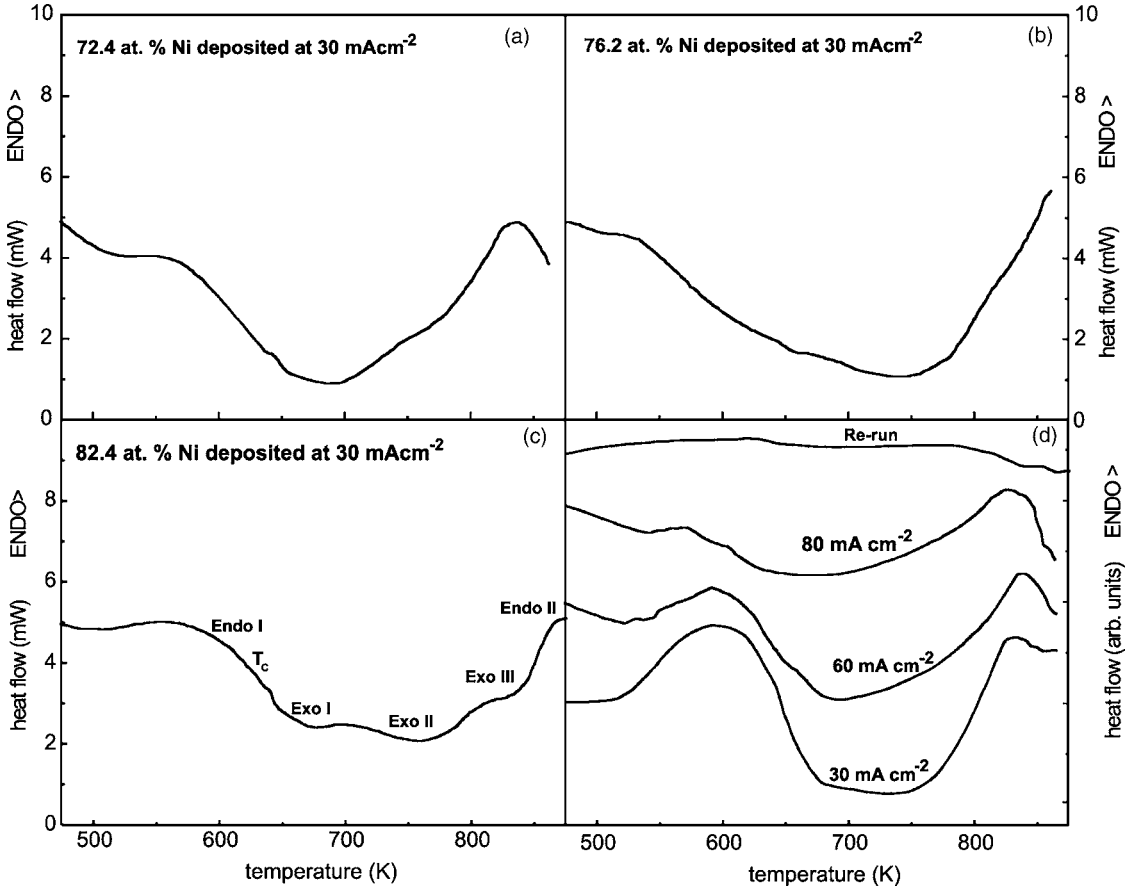

FIG. 3. Differential scanning calorimetric curves for (a) deposit No. 1 (heating rate of 10 K/min), (b) deposit No. 2 (heating rate of 10 K/min), (c) deposit No. 4 (heating rate of 5 K/min), and (d) deposit Nos. 4, 5, and 6 (heating rate of 10 K/min) and rerun of deposit 4.

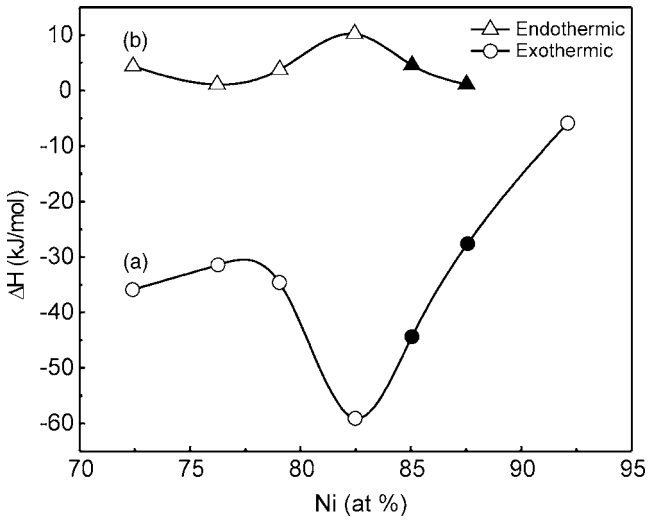

FIG. 4. (a) Exothermic and (b) endothermic energies as a function of various at. % of Ni. The continuous line is only a guide for the eye.

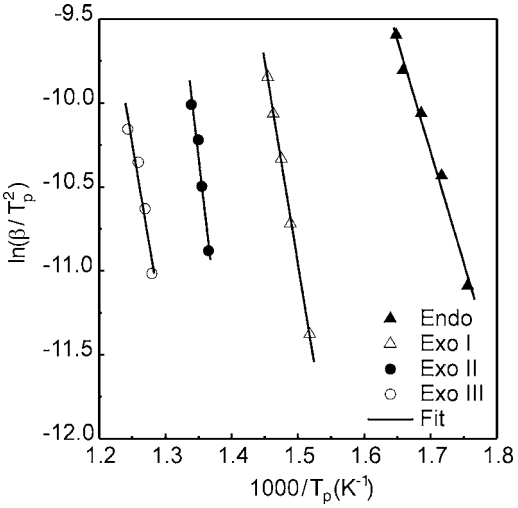

FIG. 6. The Kissinger's plot for 82.4 at. % Ni. β is the heating rate and T_P the peak temperature.

−36.2, and −6.9 kJ/mol, respectively, for the sample with 82.4 at. % Ni. The component energy values obtained for our samples is much higher than those obtained by others[18,39] for sputter deposited Ni–Mn film for a transformation to $L1_0$ structure, and the total energy is somewhat higher than the calculated enthalpies for alloy formation.[44] This higher value may be due to the nature of alloy formation in an electrodeposition technique and the process as well as extent of ordering taking place in our samples. For example, lattice defects such as screw dislocations/stacking faults are inevitable in electrodeposition.[45,46] The values above also indicate that the sample with 82.4 at. % Ni requires considerably more energy (Exo II) for ordering process than the sample with 76.2 at. % Ni, corroborating with the other results on the highly ordered state of the 76.2 at. % Ni sample. That the reordering scheme for the sample with 82.4 at. % Ni differs considerably from the 76.2 at. % Ni sample is further evidenced from the results of an *in situ* high temperature XRD (discussed later), suggesting considerable Ni segregation beyond the (DSC) reference temperature. Recently, similar segregation of Mn have also been observed in electrodeposited Ni–Mn alloys around this temperature.[47] The associated grain growths perhaps account for a larger energy of −6.9 kJ/mol for Exo III in this case. The endothermic transition (Endo II) at the end of the exothermic process [Figs. 3(a) and 3(d)] corresponds to the phase transition after ordering. The T_C from DSC agrees well with thermomagnetic results shown in Table I.

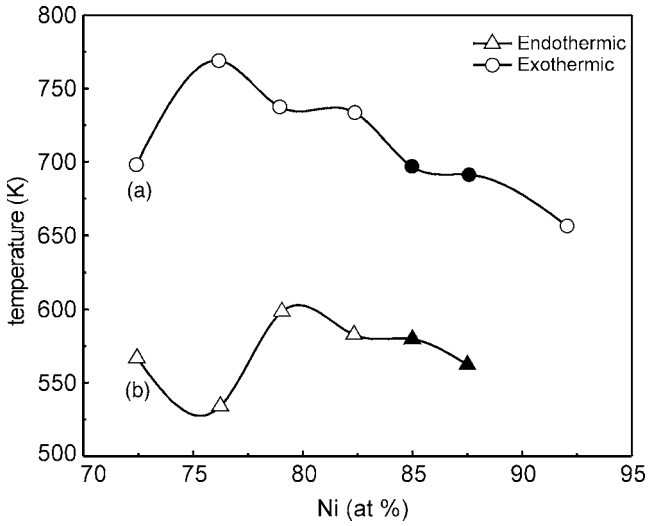

FIG. 5. (a) Exothermic and (b) endothermic peak temperatures as a function of various at. % of Ni. The continuous line is only a guide for the eye.

Figure 3(d) shows the DSC scans at a heating rate of 10 K/min of the samples from same bath deposited at CDs of 30, 60, and 80 mA cm^{-2} (deposit Nos. 4, 5, and 6 in Table I). These deposits had the compositions of 82.4, 85.8, and 87.5 at. % Ni, respectively. All the three deposits show the endothermic peak followed by a broad exothermic region and a second endothermic transition. Both the endothermic and exothermic transitions are found to be irreversible [indicated as Re-run in Fig. 3(d)]. The heat absorbed in the first endothermic process as well as the heat generated in the exothermic process decreases with CD.

Figures 4 and 5 depict the endothermic (Endo I, triangle) and exothermic (total energy, circles) peak energy values and peak temperatures, respectively, as determined from the DSC scans. In Fig. 4, the curve(a) shows a nonmonotonic trend in the variation of exothermic energy due to the ordering process with the minimum heat release for the 76.2 at. % Ni sample and the maximum for the 82.4 at. % Ni. In Fig. 5, the curve (a) shows a similar trend for the exothermic peak temperature against Ni concentration, reaching a maximum for the 76.2 at. % Ni, which in its as-deposited form is energetically close to an ordered structure. In Figs. 4 and 5, the solid triangles and solid circles correspond to deposits from the same bath as of the 82.4 at. % Ni sample but at higher CDs of 60 and 80 mA cm^{-2} yielding the compositions 85% and 87.5 at. % Ni, respectively. The emphasis here is on the Ni concentration rather than the crystallite size effect, even though the CD influences the crystallite size too. The heat absorption during hydrogen desorption [Fig. 4, curve (b)] as well as the temperature of endothermic process [Fig. 5, curve

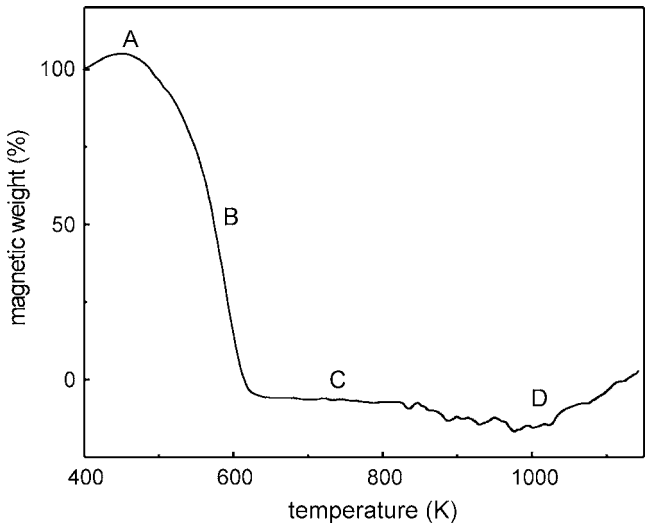

FIG. 7. The thermomagnetic curve for the 82.4 at. % Ni.

(b)] as a function of Ni concentration correlates well with the trend observed in the exothermic process. The deposit with 76.2 at. % Ni absorbs the minimum heat at the minimum temperature. The sample 92.1 at. % Ni, however, does not show any endothermic peak but only a small exothermic peak, since its structure is more corresponding to fcc than A_3B structure.[42]

The above results of exothermic energy and peak temperature variations as a function of Ni concentration clearly show that the sample with 76.2 at. % Ni possesses highest degree of ordering, whereas the one with 82.4 at. % Ni the least among all the compositions that could be obtained by electrodeposition from a wide range of bath compositions. It is noteworthy that 76.2% is close to a Ni:Mn ratio of 3:1. It is well documented that the exact composition at which Ni_3Mn ordered phase is observed, ranges between 76 and 77 at. % Ni.[42]

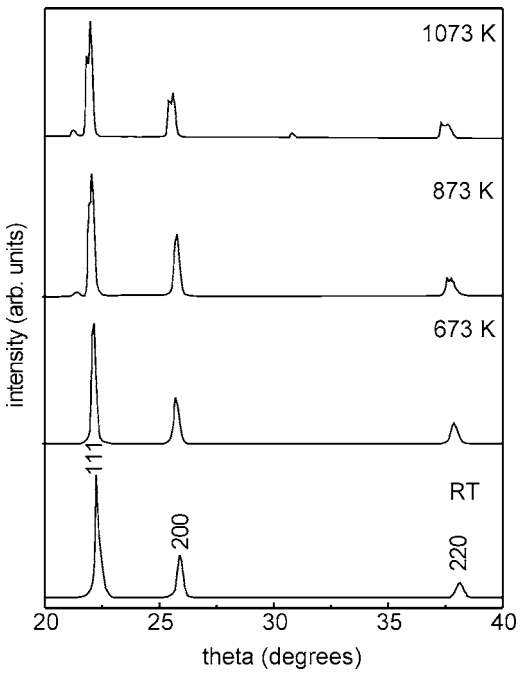

FIG. 8. *In situ* high temperature x-ray diffraction patterns for 82.4 at. % Ni.

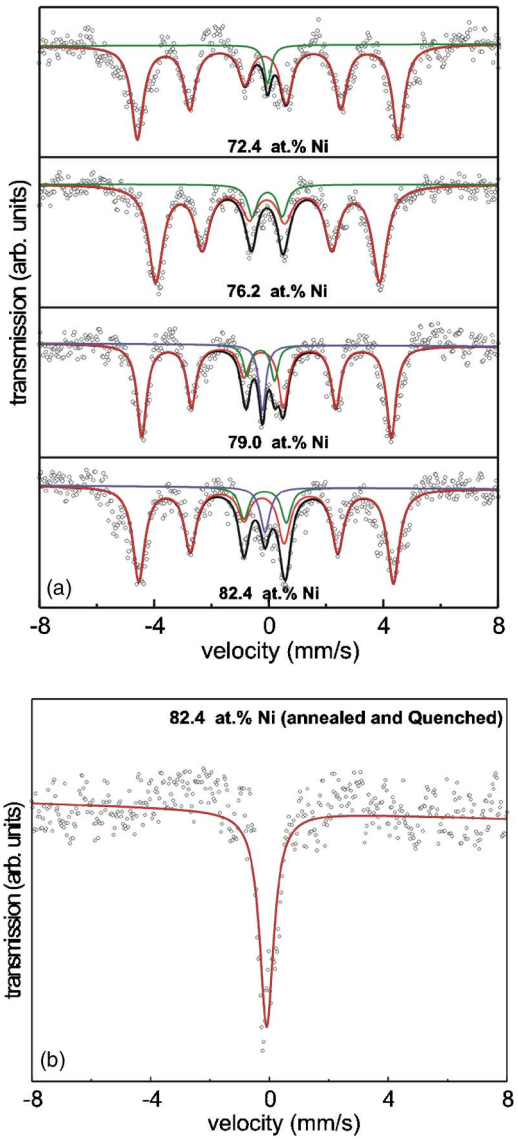

FIG. 9. (Color online) Mössbauer spectra recorded at RT for (a) 72.4, 76.2, 79.0, and 82.4 at.% Ni deposits and (b) quenched 82.4 at. % Ni deposit.

The activation energy for different stages of the ordering transformation was calculated using Kissinger analysis.[48] A number of heating rates, namely, 5, 10, 15, 20, and 25 K/min were applied to study the dependence of the peak temperature (T_P) on heating rate (β). The resulting Kissinger plots are shown in Fig. 6 for the alloy with 82.4 at. % Ni deposited at 30 mA cm^{-2} CD. From the slope of the first endothermic peak an activation energy for the dissociation of hydrogen included during alloy deposition was calculated as 106 kJ/mol. The activation energies of 200, 301, and 202 kJ/mol from the three exothermic peaks are attributed, respectively, to relaxation of defects and stresses, the long-range order transformation, and the grain growth of the nanocrystals to form microcrystals.

C. Thermogravimetric studies

A thermogravimetric magnetic curve from TGA obtained for the sample with 82.4 at. % Ni is shown in Fig. 7 as a typical example. The initial weight increase (region A in Fig.

7) is attributed to hydrogen desorption from the alloy, which induces a magnetic flux gain (due to the associated change in magnetic moments). The magnetic flux then decreases (region B) and reaches a minimum at the Curie point (T_C). The observed slow change in magnetic moment after T_C, corresponding to the region C in Fig. 7, is possibly due to the thermal energy matching the exchange energy of the ferromagnetic atom with its near-neighbor atom clusters, leading to a transition from ferromagnetic to paramagnetic phase. This is followed by region D with a small magnetic flux gain which is due to the contribution from different degrees of long-range ordering,[19] and in this 82.4 at. % Ni sample this may also be contributed in addition by segregated ferromagnetic Ni. The apparent below zero weight in the TGA trace is because of the zero reference in weight corresponding to the sample weight before hydrogen loss by desorption.

D. High temperature *in situ* XRD studies

Each of the DSC thermograms, except for the 76.2 at. % Ni sample, displays an endothermic transition beyond the exothermic process, suggesting that the ordering process is followed by a phase transition into a disordered state. In order to ascertain the onset temperature of this transition, an *in situ* high temperature XRD measurements were carried out. Figure 8 shows this for the alloy with 82.4 at. % of Ni. Starting from the temperature of 873 K [which is just above the Endo II peak temperature for this sample in Fig. 3(d)], the (111) peak exhibits a splitting, indicating the transformation of the ordered structure to a disordered structure. The lower Bragg angle component of the split (111) peak corresponds very well with the fcc-Ni and the other component is from a fcc-Ni_3Mn phase, suggesting the onset of a phase transition. The weak peaks observed in the 873 and 1073 K XRD traces of this figure correspond to $(NiO)_{0.75}(MnO)_{0.25}$ phase[49] arising due to the mild oxidation of the sample since the XRD was done in ambient conditions. It has to be noted that this onset temperature of peak splitting (873 K) agrees well with the temperatures of the second endothermic peak observed for most deposits in Figs. 3(a) and 3(d). On the other hand, it is even more significant that this second endothermic peak is not seen in the DSC scan [Fig. 3(b)] for the ordered 76.2 at. % Ni sample as also no splitting of (111) peak was observed in its *in situ* high temperature XRD patterns (not shown here), thus confirming the above conclusions on order-disorder transitions.

TABLE II. Room temperature Mössbauer parameters such as hyperfine field (H_{hf}), center (isomer) shift (CS) relative to that of α-Fe, quadrupole splitting (QS), line width (WV), and relative intensities (I_{rel}) for the various at. % of Ni.

Ni at. %	H_{hf} (kOe)	CS mm s^{-1}	QS mm s^{-1}	WV mm s^{-1}	I_{rel}
72.4	282	0.04	−0.07	0.50	85
	0	−0.13	−0.97	0.60	7.5
	0	0.11	0	0.60	7.5
76.2	241.9	0.06	−0.02	0.60	90
	0	0.06	1.05	0.40	10
79.0	269.6	−0.01	−0.09	0.40	80
	0	−0.17	−0.97	0.30	10
	0	−0.11	0	0.30	10
82.4	275.2	−0.02	−0.07	0.50	81.6
	0	−0.01	−1.47	0.40	10.9
	0	0.01	0	0.40	7.4
Quenched	0	0.07	0	0.58	100

E. Mössbauer studies

Figure 9 shows the Mössbauer spectra obtained at RT for deposits with 72.4, 76.2, 79.0, and 82.4 at. % Ni (deposit Nos 1, 2, 3, and 4). The spectra were fitted using a least squares method and the values of the fitted parameters are given in Table II. The fitting yielded one sextet, one doublet, and a singlet for all samples except for 76.2 at. % Ni, for which the singlet was absent. The sextet corresponds to the long-range order (ferromagnetic phase) and the singlet of lower intensity to the short-range order (paramagnetic

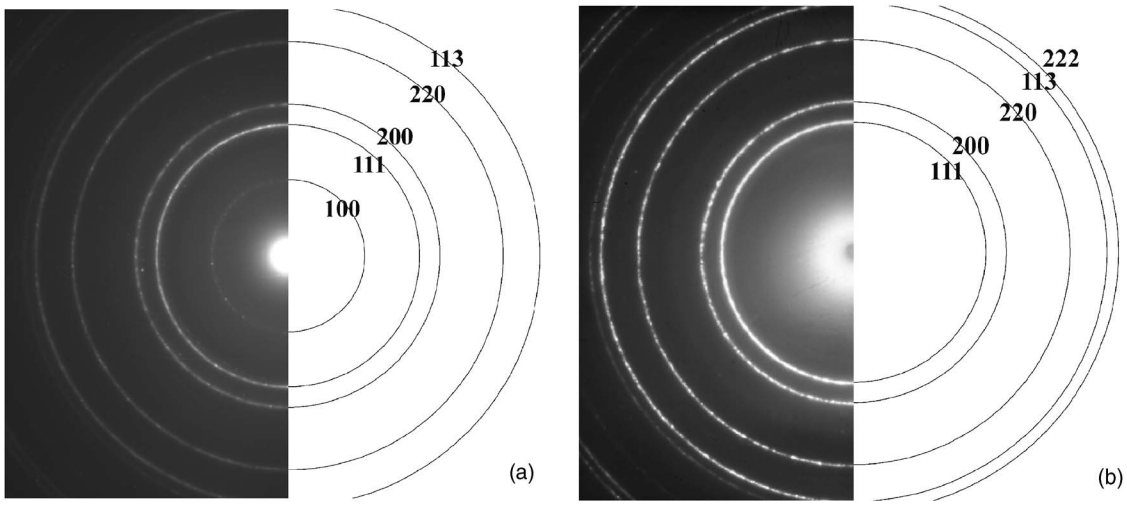

FIG. 10. TEM selected area diffraction (SAD) patterns for the 76.2 at. % Ni (a) and 82.4 at. % Ni (b) films. The analysis of the TEM diffraction patterns was based on the software PROCESS DIFFRACTION (Ref. 54).

phase). An asymmetry in the sextet pattern noticed for all the deposits is due to the inclusion of hydrogen[50] which occupies the octahedral sites of the fcc lattice in nickel[51] and palladium.[52] The introduction of hydrogen reduces the average magnetic moment of the nickel atom, lowering the Curie temperature as well as the hyperfine interaction of the iron atom. The doublet arises due to the presence of a quadrupole splitting, thus indicating an asymmetry in the environment around the resonant Fe atoms[22] or the presence of a nonmagnetic impurity.

For Ni concentrations other than 76.2 at. % Ni, the fitting of the spectra indicates the coexistence of two phases, one giving rise to a well-resolved sextet and another yielding the less intense paramagnetic singlet at room temperature. This perhaps suggests the presence of a small number of short-range ordered domains in a matrix of long-range order, in agreement with literature results on bulk samples.[22,53] Fe nuclei in these two phases experience different hyperfine fields and the corresponding Curie transitions are different. The T_C of the short-range order phase is presumably below room temperature and could be determined only with low temperature Mössbauer studies. It can be argued that the singlet may be due to the superparamagnetic nature of the smaller crystallites, however, it is missing in 76.2 at. % Ni deposit. The minimum of hyperfine field (H_{hf}) occurring for 76.2 at. % Ni sample suggests that the short-range ordered paramagnetic phase is absent in 76.2 at. % Ni sample. In order to ascertain the disordered phase in 82.4 at. % Ni sample at 1073 K (as suggested from *in situ* high temperature XRD), sample was annealed at 1073 K for 24 h and was quenched in air. The Mössbauer spectrum of this sample [Fig. 9(b)] shows a well-defined singlet, confirming the disordered paramagnetic phase.

F. Superlattice ordering

The conclusion about the presence of a long-range ordering in the 76.2 at. % Ni sample and its absence in at least the 82.4 at. % Ni sample arrived at from the various studies above was more clearly established by the analysis of the selected area diffraction (SAD) patterns obtained from TEM experiments. Figures 10(a) and 10(b) show these SAD patterns for the as-deposited 76.2 at. % Ni and 82.4 at. % Ni samples, respectively. The diffraction from the sample with 76.2 at. % Ni [Fig. 10(a)] yields the (100) ring apart from the other fcc rings. The presence of the normally forbidden (100) inner ring is an indication of the existence of an $L1_2$-type ordering, thus giving rise to a superlattice structure along the [001] direction. No such long-range ordering was, however, found in the 82.4 at. % Ni sample, as confirmed by the lack of this (100) superlattice ring in Fig. 10(b).

IV. CONCLUSION

Electrodeposited Ni–Mn alloys formed within a narrow compositional range, in spite of employing a wide range of bath composition. The films of Ni_3Mn had a nanocrystalline fcc structure, determined by XRD studies. An analysis of the DSC scans revealed that the process of ordering in the alloys takes place via three distinct stages, namely, relaxation of defects and stresses, progression of a long-range order transformation, and grain growth with activation energies of 200, 301, and 202 kJ/mol, respectively. While the minimum exothermic energy value and a high T_C exhibited by the deposit with 76.2 at. % Ni along with the absence of any short-range ordered paramagnetic phase for this sample as revealed by Mössbauer studies indicate that this composition enjoys a high degree of ordering even in the as-deposited condition, the superlattice reflections observed in SAD exclusively for this 76.2 at. % Ni case establishes that this ordering is of $L1_2$ type. Though some degree of ordering was visible for the electrodeposited Ni–Mn alloys with Ni ranging from 72.6 to 87.5 at. %, the alloy with 76.2 at. % Ni was the most stable with pure ferromagnetic phase.

ACKNOWLEDGMENTS

The author (A.S.) wishes to acknowledge the UNESCO and ICTP-TRIL, Trieste for his TRIL fellowship. He also thanks Professor G. Furlan, ICTP-TRIL, for his encouragement and support.

[1] J. J. Kelly, S. H. Goods, and N. Y. C. Yang, Electrochem. Solid-State Lett. **6**, C88 (2003).
[2] S. Gunan and B. J. Nelson, J. Magn. Magn. Mater. **292**, 49 (2005).
[3] S. H. Goods, J. J. Kelly, and N. Y. C. Yang, Microsyst. Technol. **10**, 498 (2004).
[4] T. Lin, D. Mauri, N. Staud, C. Hwang, J. K. Howard, and G. L. Gorman, Appl. Phys. Lett. **65**, 1183 (1994).
[5] S. Mao, S. Gangopadhyay, N. Amin, and E. Murdock, Appl. Phys. Lett. **69**, 3593 (1996).
[6] T. Krenke, E. Duman, M. Acet, E. F. Wassermann, X. Moya, L. Manosa, and A. Planes, Nat. Mater. **5**, 450 (2005).
[7] G. H. Zhou and H. Bakker, Acta Metall. Mater. **42**, 3009 (1994).
[8] V. S. Rachinskas, V. A. Parfenov, and L. V. Orlovskaya, Elektrokhimiya **30**, 243 (1994).
[9] J. Ho and K. Lin, Scr. Metall. Mater. **33**, 1895 (1995).
[10] N. Atanassov and V. Nfitreva, Surf. Coat. Technol. **78**, 144 (1996).
[11] S. Jayakrishnan and S. R. Natarajan, Met. Finish. **78**, 23 (1991).
[12] C. Kollia, N. Spyrellis, J. Abnbland, M. Froment, and G. Murin, J. Appl. Electrochem. **20**, 1025 (1990); P. Pouderox, I. Chassaing, J. P. Bonino, and A. Rousset, Surf. Coat. Technol. **45**, 161 (1991).
[13] H. K. Srivastava, Mater. Sci. Forum **93**, 20 (1995).
[14] A. Stephen, M. Ilango, T. Nagarajan, and M. V. Ananth, Trans. Inst. Met. Finish. **76**, 111 (1998).
[15] M. D. Baro, S. Surinach, J. Malagelada, M. T. Clavaguera-Mora, S. Gialanella, and R. W. Cahn, Acta Metall. Mater. **41**, 1065 (1993).
[16] G. H. Zhou, M. J. Zwanenburg, and H. Bakker, J. Appl. Phys. **78**, 3438 (1995).
[17] A. R. Yavari, P. Crespo, E. Pulido, A. Hernando, G. Fillion, P. Lethuillier, M. D. Baro, and S. Surinach, in *Ordering and Disordering in Alloys*, edited by A. R. Yavari (Elsevier, London, 1992). p. 12.
[18] M. Huang, J. Appl. Phys. **97**, 64906 (2005).
[19] M. J. Marcinkowski and N. Brown, J. Appl. Phys. **32**, 375 (1961).
[20] M. J. Marcinkowshi and R. M. Poliak, Philos. Mag. **8**, 1023 (1963).
[21] A. Paoletti, F. P. Ricci, and L. Passar, J. Appl. Phys. **37**, 3236 (1966).
[22] G. Chandra and T. S. Radhakrishnan, Phys. Status Solidi **40**, 267 (1970).
[23] S. Kaya and M. Nakayama, Proc. Phys.-Math. Soc. Japan **22**, 126 (1940).
[24] C. G. Shull and M. K. Wilkinson, Phys. Rev. **97**, 1746 (1955).
[25] J. W. Cable and H. R. Child, Phys. Rev. B **10**, 4607 (1974).
[26] G. Mazzone, C. Petrillo, and F. Sacchetti, Phys. Rev. B **49**, 4307 (1994).
[27] M. J. Marcinkowski and R. M. Poliak, Philos. Mag. **8**, 1023 (1963).
[28] S. Senoussi and Y. Oner, J. Appl. Phys. **55**, 1476 (1984).
[29] C. D. Keener and M. B. Weissman, Phys. Rev. B **49**, 3944 (1994).
[30] A. Kilic, Y. Oner, and H. Celik, J. Magn. Magn. Mater. **146**, 298 (1995).
[31] J. S. Kouvel, W. Abdul-Razzaq, and Kh. Ziq, Phys. Rev. B **35**, 1766 (1987).
[32] M. Hennion, B. Hennion, I. Mirebeau, S. Lequien, and F. Hippert, J. Appl. Phys. **63**, 4071 (1988).

[33]T. Sato, T. Ando, T. Watanabe, S. Itoh, Y. Endoh, and M. Furusaka, Phys. Rev. B **489**, 006074 (1993).
[34]T. Ogawa, H. Nagasaki, and T. Sato, J. Magn. Magn. Mater. **246**, 169 (2002).
[35]S. Kaya and A. Kussmann, Z. Phys. **72**, 293 (1935).
[36]S. K. Sidorov and A. V. Doroshenko, Phys. Status Solidi **16**, 737 (1966).
[37]A. Stephen, T. Nagarajan, and M. V. Ananth, Mater. Sci. Eng., B **55**, 184 (1998).
[38]A. Stephen, M. V. Ananth, V. Ravichandran, and B. R. V. Narashiman, J. Appl. Electrochem. **30**, 1313 (2000).
[39]P. F. Ladwig, Y. Yang, L. Ding, I. Tsu, and Y. A. Chang, J. Electron. Mater. **32**, 115 (2003).
[40]S. Harada, T. Sohmura, and F. E. Fujita, J. Phys. F: Met. Phys. **13**, 1429 (1983).
[41]R. A. Dunlap and K. Dini, J. Phys. F: Met. Phys. **14**, 2797 (1984).
[42]T. B. Massalshi, *Binary Alloy Phase Diagrams* (ASM International, Metal Park, OH, 1992), Vol. 3, p. 2582.
[43]G. H. Zhou and H. Bakker, Phys. Rev. B **49**, 12507 (1994).
[44]A. K. Niessen, F. R. de Boer, R. Boom, P. F. de Châtel, and W. C. M. Mattens, CALPHAD: Comput. Coupling Phase Diagrams Thermochem. **7**, 51 (1983).
[45]R. W. Hiton, L. H. Schwartz, and J. B. Chohen, J. Electrochem. Soc. **110**, 103 (1963).
[46]N. V. Parthasaradhy, *Practical Electroplating Handbook* (Prentice-Hall, Englewood Cliffs, 1989), p. 54.
[47]E. A. Marquis, A. A. Talin, J. J. Kelly, S. H. Goods, D. N. Seidman, and M. K. Miller, Microsc. Microanal. **11**, 890 (2005).
[48]H. E. Kissinger, Anal. Chem. **29**, 1702 (1957); J. Res. Natl. Bur. Stand. **57**, 217 (1956).
[49]JCPDS-International Centre for Diffraction Data, PDF-2 Database No. 78-0425 (2003).
[50]G. K. Wertheim and D. N. E. Buchanan, J. Phys. Chem. Solids **28**, 225 (1967).
[51]E. O. Wollan, J. W. Cable, and W. C. Koehler, J. Phys. Chem. Solids **24**, 1141 (1963).
[52]J. E. Worsham, M. K. Wilkinson, and C. G. Shull, J. Phys. Chem. Solids **3**, 303 (1957).
[53]T. S. Radhakrishnan, Ph.D. thesis, University of Bombay, 1973.
[54]J. L. Labar, Ultramicroscopy **103**, 237 (2005).